Nanoscale

COMMUNICATION

Palladium / Cobalt Nanowires with Improved Hydrogen Sensing Stability at Ultra-Low Temperatures

Received 00th January 20xx,
Accepted 00th January 20xx

DOI: 10.1039/x0xx00000x

Lingling Du,[a] Dongliang Feng,[a] Xiaxia Xing,[a] Yang Fu,[a] Luis F Fonseca [b] and Dachi Yang *[a]

The metallic dopants in palladium (Pd) sensing materials enable the modification to the d-band electrons of Pd, which is expected to tune the α-β phase transitions of PdH_x intermediate, and thus improving the sensing stability to hydrogen. Here, the boosted hydrogen-sensing stability at ultra-low temperatures has been achieved with palladium / cobalt nanowires (PdCo NWs) as the sensing material. The various Co contents in PdCo NWs are modulated via AAO-template-confined electrodeposition. The temperature - dependent sensing evaluations were performed in 0.1-3 v/v% hydrogen. Such sensors integrated with PdCo NWs are able to stably detect hydrogen as low as 0.1 v/v%, even the temperature is lowered to 273 K. Additionally, the critical temperatures of "reverse sensing behavior" of the PdCo NWs ($Pd_{82}Co_{18}$: T_c = 194 K, $Pd_{63}Co_{37}$: T_c = 180 K, $Pd_{33}Co_{67}$: T_c = 184 K) are observed much lower than that of pristine Pd NWs (T_c = 287 K). Specifically, the $Pd_{63}Co_{37}$ NWs (~37 at% Co content) sensor shows outstanding stability of sensing hydrogen against α-β phase transitions within the wide temperature range of 180 - 388 K, which is attributed to both the electronic interaction between Pd and Co, and the lattice compression strain caused by Co dopants. Moreover, the "reverse sensing behavior" of PdCo NWs is explicitly interpreted by using the α-β phase transitions model.

Introduction

Hydrogen (H_2) is a green, sustainable and high-energy carrier in the growing hydrogen economy.[1, 2] However, the flammable and explosive nature of H_2 challenges its practical applications.[3, 4] Hence, a reliable and stable sensor is of considerable importance to safety issues.[5] Pd and its alloys have been intensively studied for hydrogen detection and hydrogen related catalytic reactions as molecular hydrogen easily dissociates on the surface of Pd with low activation barrier.[6-8] Meanwhile, the hydrogen atoms permeate into the metallic lattice to form PdH_x intermedium,[9] inducing an electrical resistance change in a reversible manner at moderated temperatures (< 200°C).[10] In fact, most of the room-temperature hydrogen sensors employ pristine Pd or its alloys as sensing materials.[3, 11, 12]

Generally, PdH_x features the interstitial solid solution (α phase, x < 0.01) and Pd hydride (β phase, x > 0.7), and the two phases coexist for 0.01<x<0.7 in bulk.[13, 14] However, the interstitial H atoms in the Pd lattice (PdH_x) both perturb the electron flow and expand the volume of the solid,[15-17] which generally results in two hydrogen sensing mechanisms, identified as electron scattering ($\Delta R_H > 0$ in α phase) and hydrogen-induced lattice expansion ($\Delta R_H < 0$ in β phase), respectively.[18] The two sensing mechanisms are in conflict and counteraction, and thus deteriorate the performance of hydrogen sensors.[18] Moreover, counteraction and mutual cancellation bring temperature-dependent sensing behaviour in Pd-based nanowires (NWs) sensors with a critical temperature, in which the sensor response is minimal due to a switch on the dominant sensing mechanism, here referred as "reverse sensing behavior".[19] The dual-switching response to H_2 of ultra-small grained Pd nanopattern becomes too weak to be detected during α-β phase transition.[20]

Additionally, multiple α-β phase transitions of the PdH_x intermedium induced by the hydrogen concentration and the operating temperature, cause mechanical stress on the resistor, resulting in deformation and delamination.[21, 22] Upon repeated exposure to H_2, Pd films suffer from buckling and peeling.[23, 24] Pd NWs prepared from EDTA-contained plating solution have demonstrated that the compact nanograins enable the Pd NWs to be less prone to fracture, even repeated exposure to 10% H_2.[25, 26] Meanwhile, one-dimensional (1D) nanostructures efficiently alleviate swelling stress from hydrogenation.[27-29] Moreover, previous investigations suggest that Pd alloys

[a] Department of Electronics, College of Electronic Information and Optical Engineering, Nankai University, Tianjin 300350, China.
E-mail: yangdachi@nankai.edu.cn
[b] Department of Physics, University of Puerto Rico Rio Piedras, San Juan, PR 00931, USA.

†Electronic Supplementary Information (ESI) available. See DOI: 10.1039/x0xx00000x

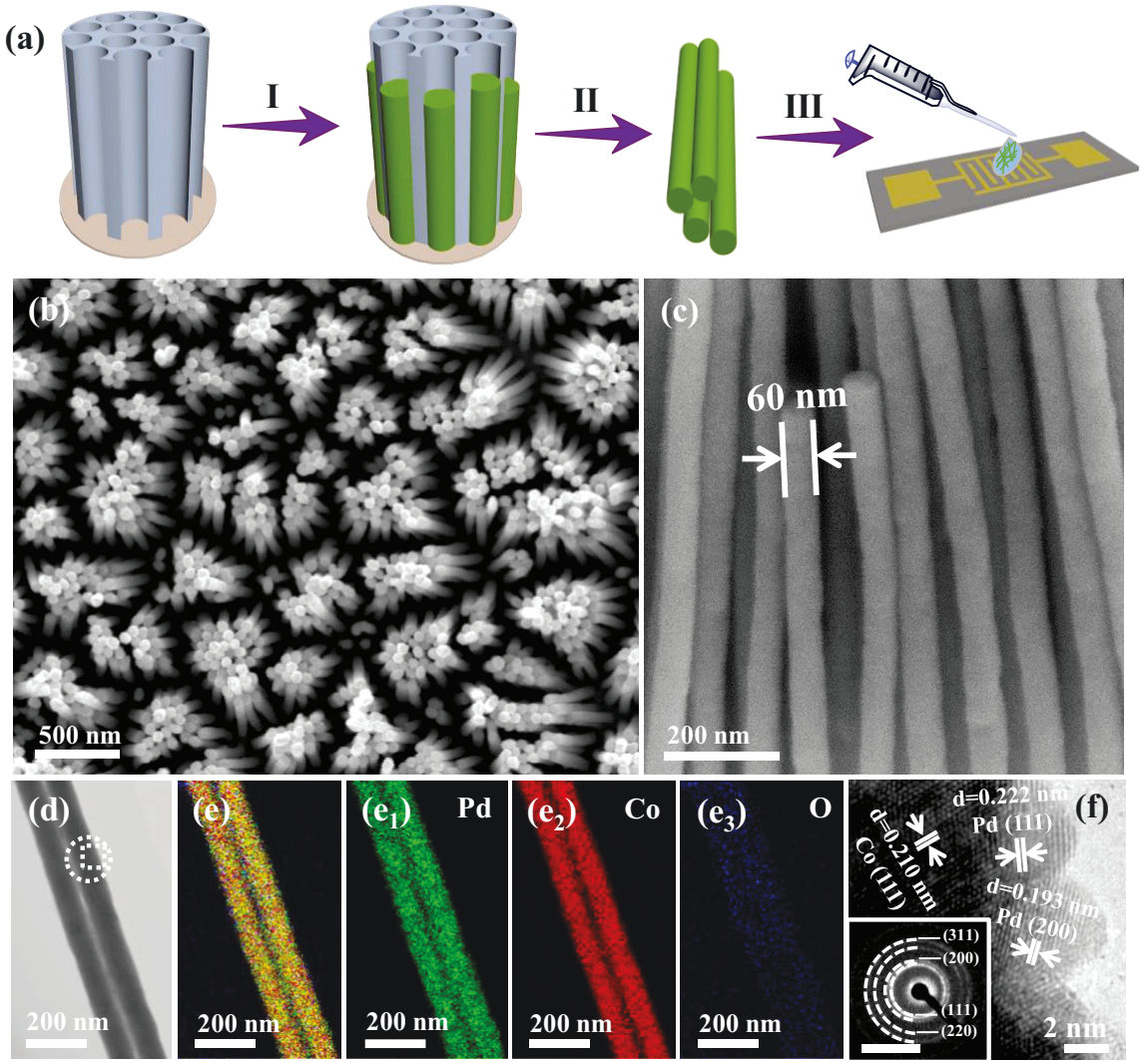

Fig. 1 (a) Schematic synthesis and integration of PdCo NWs including (Ⅰ) electrodeposition, (Ⅱ) removal of AAO and (Ⅲ) integration. (b) Top-view and (c) side-view SEM images of PdCo NWs arrays. (d) TEM image of representative dual PdCo NWs, the overlapped (e) and the separated elemental mappings (e1) Pd, (e2) Co and (e3) O. (f) HR-TEM image with the inset SAED pattern taken from the dashed rectangle and circle in (d), respectively. The scale bars in inset (f) is 1 / (10 nm).

practical applications of hydrogen sensors. Furthermore, one of the most important requirements for such sensors is the ability to stably work over wide temperature range, either in extremely cold environments (e.g., liquid hydrogen tanks and pipes), or in much warmer devices (e.g., membrane and fuel cell).[22] Especially, hydrogen is used as a cryogenic fuel in rockets, where it is required to detect hydrogen leakage at temperature around 260 K.[22] Though the hydrogen sensing materials of metal oxides modified with noble metals (e.g., Pd, Pt and Au) [36-39] show superior sensitivity, selectivity and low detection limit, of which the stability is highly dependent on the working temperature, hence those with high stability are desired at low-temperature environments.

oxide (AAO), and further integrated onto the inter-digital electrodes (IED) to build sensors. The PdCo NWs sensors presented stable sensing response to H_2 in a wide temperature range. Especially, the critical temperature related to the "reverse sensing behaviour" of the $Pd_{63}Co_{37}$ NWs sensors lowered to 180 K in contrast with that of pristine Pd NWs at 287 K. The outstanding hydrogen-sensing stability at low temperatures is related to the synergistic effect of the electron modification and the lattice compression strain on Pd-based alloy via cobalt doping, which inhibit the α-β phase transition in PdH_x.

Results and discussion

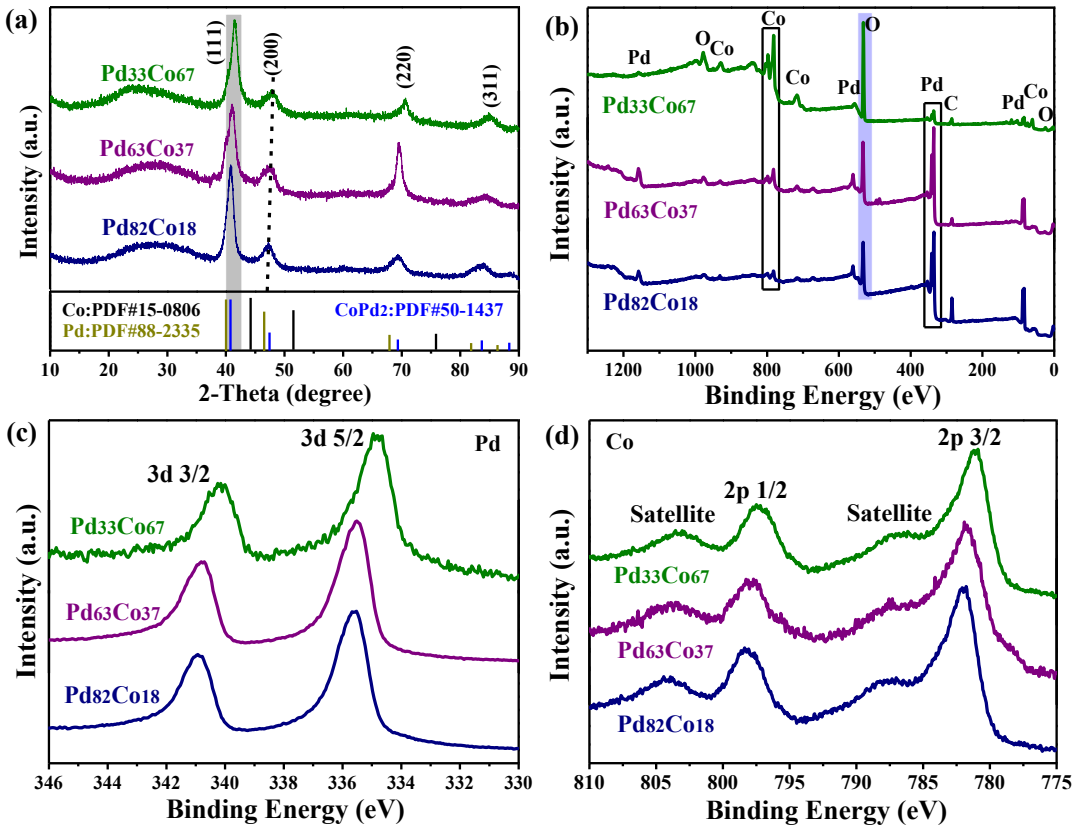

Fig. 2 (a) XRD patterns, (b) XPS survey spectra and the high-resolution XPS spectra of (c) Pd 3d and (d) Co 2p of PdCo NWs with various Co atomic ratios, respectively.

Figure 4. (a) XRD of PdCo NWs with various Co atomic ratio. (b) XPS fully scanned spectra of PdCo NWs with various Co atomic ratio. The XPS spectra of the Pd 3d region (c) and the Co 2p region (d) for PdCo NWs with various Co atomic ratio, respectively.

Morphologi and

The scanni
shows the
arrays, ind
image in F at the
uniform cy cated
templates.

ratio assisting hydrogen adsorption. The transmission electron microscopy (TEM) image (Figure 1(d)) taken from two contiguous PdCo NWs further confirms the similar geometrical parameters of the NWs. The corresponding (energy dispersive X-ray spectroscopy (EDS) elemental mappings (Figure 1(e)) illustrate that Pd (Figure 1(e_1)) and Co (Figure 1(e_2)) distribute homogeneously along the NWs. Oxygen content (Figure 1(e_3)) is unavoidable due to the fact that electrodeposition was performed in atmospheric environment, which is consistent with the XPS observation described below.

The detailed surface of PdCo NWs is further seen in the high resolution TEM (HRTEM) image (Figure 1(f)). Specifically, the lattice fringes with spacing of 0.222 and 0.193 nm are indexed to the (111) and (200) planes of Pd (PDF#88-2335), respectively. Also, the lattice spacing of 0.210 nm matches well with the (111) planes of Co (PDF#15-0806). Meanwhile, the selective area electron diffraction (SAED) pattern (inset of Figure 1(f)) shows bright diffractive rings, suggesting the polycrystalline nature of the NWs. Practically, the chemical content of palladium/cobalt in NWs were primarily modulated by tuning the molar ratio of the precursors in the electrolytes. According to the atomic ratio from EDS analysis (Figure S1, Supporting information), these as-

between these indexed to (111), (200), (220), (311) planes of face-centered cubic Pd (PDF#15-0806) and Co (PDF#882335), which further indicates the formation of PdCo alloy. Additionally, the crystallite sizes were evaluated using the classical Scherrer formula to the major diffractive peaks [40]:

$$D = K\lambda/(\beta \cos\theta) \quad (1)$$

where, D is the average crystallite size, λ is the wavelength of the X-ray radiation (Cu Ka = 0.15418 nm), K is the Scherrer constant (0.89) for spherical shape, β is the full width at half-maximum height (FWHM), and θ is the Bragg diffraction angle.[41] The calculated results are summarized in Table S1 of the Supporting information. It can be seen that the grain size increases with the increase of Co content. Meanwhile, the diffractive peaks shift positively, revealing that the lattice contraction. As previously reported,[42, 43] the lattice stress of Pd alloys may suppress the excessive expansion of the PdHx intermediate to relieve Pd lattice of the deformation, which lies the foundation for the hydrogen-sensing stability at low temperature.

The X-ray photoelectron spectroscopy (XPS) spectra of PdCo NWs in Figure 2(b) suggest the existence of Pd, Co, O and C elements, in which the C element may arise from

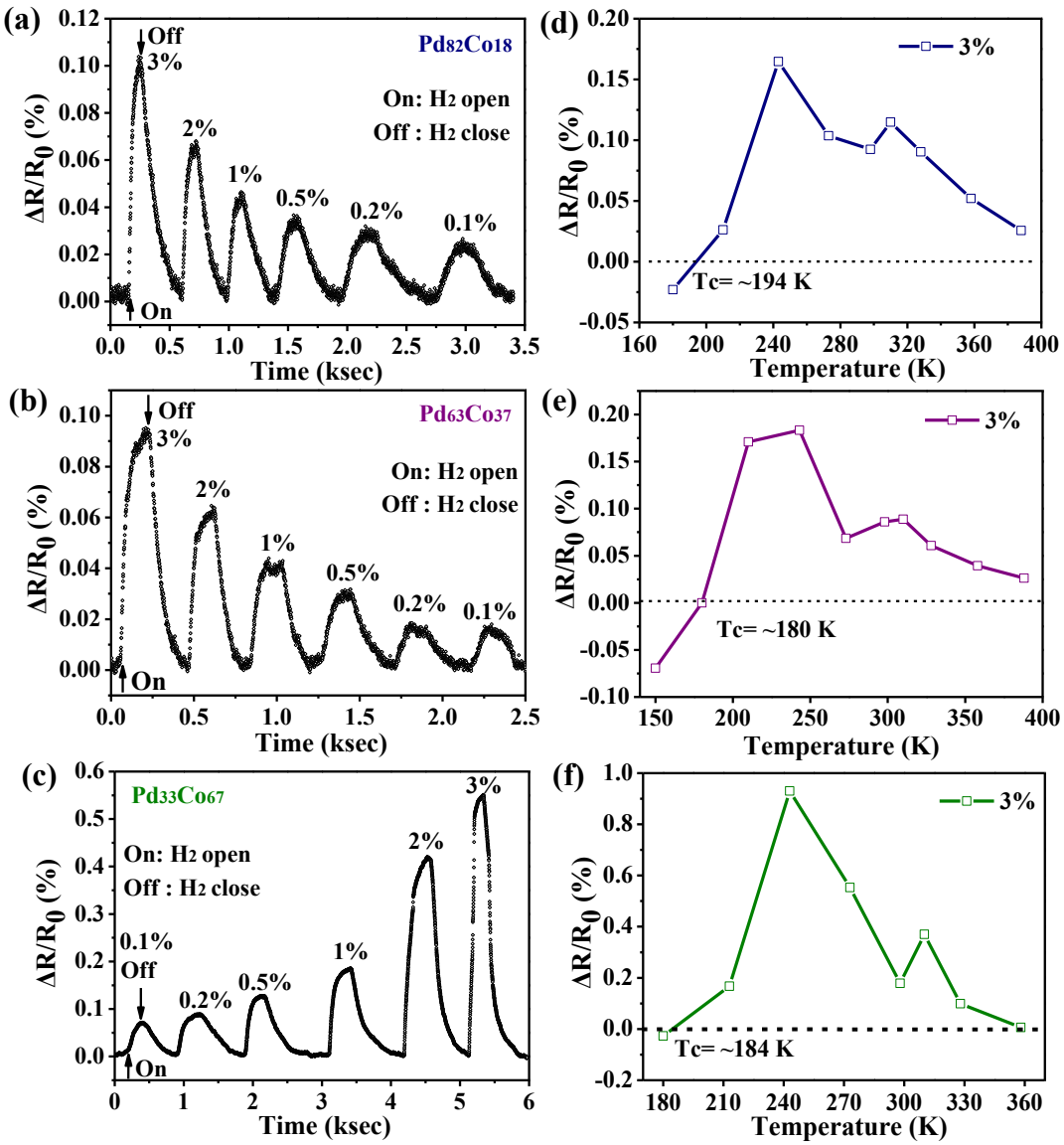

Fig. 3 (a)
(f) $Pd_{33}C$

contai
intens
conte
show
respec
Co 2p, we observed the Pd 3d BEs in PdCo NWs are negatively shifted along with the increasing Co content, which is consistent with the fact that the Co 2p BEs are positively shifted along with the increasing Pd content. The phenomenon is mainly ascribed to the electron interaction between Pd and Co, which implies that the electrons transfer from Co to Pd. Such electron-rich state in Pd may assist hydrogen adsorption and dissociation. Consequently, the electron d-band of Pd is modified by alloying with cobalt, which is expected to improve its sensing stability at low temperature.

Hydrogen sensing stability

desorption achieves baseline resistance. It has been reported that the "reverse sensing behaviour" for pristine Pd NWs occurs at 287 K,[19] which greatly degraded the sensing stability to hydrogen. Apparently, the critical temperature of the "reverse sensing behaviour" of PdCo NWs is far below 273 K; accordingly, the stable working temperature-range is widened.

Figures S2(a) - (f) in the Supporting information further display the response time (T_{res}) and the recovery time (T_{rec}) of those sensors to 3% and 1% H_2 at 273 K, respectively. Compared to other two sensors, the $Pd_{63}Co_{37}$ NWs sensor presents both faster response to H_2 (T_{res} ~ 85 s to 0.1% / T_{res} ~ 90 s to 3%) and quicker hydrogen desorption process (T_{rec} ~ 200 s to 0.1% / T_{rec} ~170 s to 3%). By contrast, the $Pd_{33}Co_{67}$ NWs sensor shows

Table 1. The critical temperature of various Pd-based NWs sensors

Sensors	The critical temperature (Tc)	R_H (+) mode response working temperature range	R
Single Pd NW	263 K	263-370 K	[illegible]
Multiple Pd NWs	287 K	287-370 K	[illegible]
P-PdCu	264.2 K	264.2-370 K	[illegible]
PS-PdCu	257.2 K	257.2-370 K	[illegible]
PM-PdCu NWs	239.9 K	239.9-370 K	[illegible]
screw-threaded PdCu	259.4 K	259.4-370 K	[illegible]
random-gapped PdCu	261 K	261-370 K	44
RS-PdBi	194.3 K	194.3-400 K	45
$Pd_{33}Co_{67}$	184 K	184-358 K	This work
$Pd_{82}Co_{18}$	194 K	194-388 K	This work
$Pd_{63}Co_{37}$	180 K	180-388 K	This work

higher sensing response (Figure 3(c)) and slower T_{res} and T_{rec} (Figure S2(e)-(f), Supporting information), which is caused by the affinity adsorption of oxides to the dissociated hydrogen. Large amounts of oxides are formed in $Pd_{33}Co_{67}$ NWs during electrodeposition due to the oxyphilicity of cobalt, which is testified by the XPS characterization (Figure 2(b)).

The effect of affinity adsorption of oxides on hydrogen-sensing performance was further explored when elevating the temperature. Figures S3 – S5 in the Supporting information show the response to hydrogen of the three sensors at the 298 - 388 K temperature range. We should point that when the $Pd_{33}Co_{67}$ sensor was exposed to H_2 at 388 K (Figure S5(e), Supporting information), an increase in electrical resistance value followed by a decrease was observed, which could be ascribed to the reduction of cobalt oxides. Firstly, the hydrogen atoms dissociated by palladium diffuse into the NWs inducing the electrical resistance increase, and then the cobalt oxides reduce to metallic cobalt by the dissociated hydrogen at the high temperature that leads to the decrease in resistance. As indicated, the excessive content of oxygen in Pd-alloyed NWs is unfavourable for H_2 detection at high temperatures. By comparison, the $Pd_{82}Co_{18}$ and $Pd_{63}Co_{37}$ sensors show more stable response to hydrogen at those temperatures. To investigate the repeatability of these sensors, they were exposed to various concentrations of hydrogen over multi-cycles at room temperature. As a consequence, the constant response under same concentration with tiny variation was observed (Figure S3(f), S4(f) and S5(f), Supporting information), suggesting the outstanding repeatability for PdCo sensors.

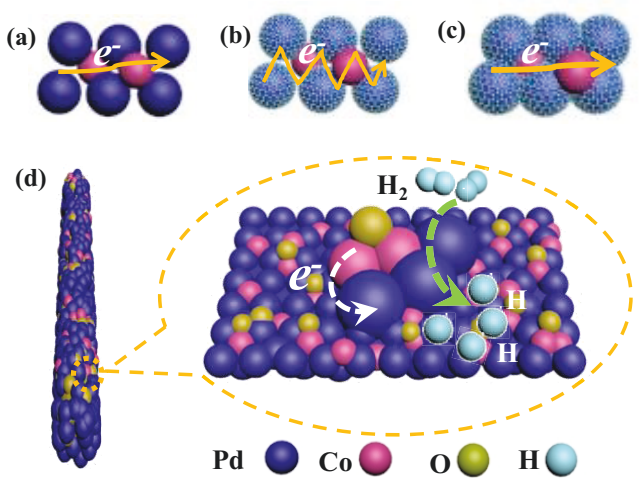

Fig. 4 (a) - (c) The scheme on hydrogen sensing mechanism of "reverse sensing behavior". (d) The schematic diagram of stable hydrogen sensing for PdCo NWs at low temperature.

As known, the "reverse sensing behaviour" and multiple α-β phase transitions of PdHx intermedium cause lattice deformation and trigger poor sensing stability.[21,22,29] To further investigate the low-temperature sensing performance of PdCo NWs, the operating temperature was lowered until the "reverse sensing behaviour" occurred (Figures S6 - S8, Supporting information). Notably, these sensors still rely on the R_H (+) mode for their response to H_2 at temperature as low as 243 K (Figures S6(a), S7(a) and S8(a) in Supporting information). The dependence of the hydrogen response on temperature is summarized in Figures 3(d) - (f), from which one can see that the response signals become weak as the operating temperature approaches the critical temperature (T_c). After further lowering the temperature, R_H (-) mode response was observed (Figures S6(c), S7(d) and S8(b), Supporting information), opposite to the response at higher temperatures. Similarly, such reverse hydrogen-sensing behaviours have been reported in other Pd-base NWs sensors listed in Table 1. In comparison, the critical temperature of $Pd_{63}Co_{37}$ sensor (T_c = ~180 K) is far lower than those reported in previous studies,[19, 29, 44, 45] which means the hydrogen sensor can stably work over a wider temperature range. Meanwhile, the hydrogen-selective evaluation demonstrates that the $Pd_{63}Co_{37}$ NWs sensor hardly response to the interfering gases, suggesting the excellent selectivity to H_2 (Figure S9, Supporting information). Additionally, the hydrogen-sensing performance of pure Co NWs was studied and no electrical resistance variation was observed when pure Co NWs were exposed to H_2 at various temperatures (Figure S10, Supporting information). To summarize, pure Co NWs have no hydrogen-sensing performance, while the Pd-alloyed NWs with Co greatly improve the sensing stability to hydrogen at low temperature.

Hydrogen sensing model

The α-β phase transition has been reported to explain the dual-switching H_2 response of the ultra-small grained Pd nanopattern. [20] Similarly, the temperature-dependent "reverse

sensing behaviour" of PdCo NWs is schematically illustrated in Figures 4(a) - (c). The electrodeposition enables interconnected conductive grains formation inside of PdCo NWs (Figure 4(a)). On exposure to H_2, the dissociated H atoms on the surface of Pd diffuse into the Pd lattice (α-phase PdH_x), acting as the electron scattering centers, and thus increase the electrical resistance (Figure 4(b)). While lowering the temperature, more H atoms are adsorbed onto Pd atoms (β-phase PdH_x) due to lower diffusion rate, leading to lattice volume expansion that shortens the interface gaps of grains between bumps on the surface of PdCo NWs. Thus, the final formation of new conductive pathways by gaps closing reduces the resistance, which further interprets the "reverse sensing behaviour" at low temperature (Figure 4(c)).

To gain insight into the lowered critical temperature of PdCo NWs, the mechanism is schematically described in Figure 4(d). Firstly, when Co species dopes into Pd lattice, the lattice compression occurs, testified via the above XRD characterization (Figure 2(a)), which results in lattice stress. As known, the alloyed lattice is less altered by hydrogen uploading due to the lattice stress and thus becomes less brittle than pure Pd lattice,[42] which is an important factor of low-temperature durability. Further, as suggested by the XPS analysis, electrons transfer from Co species to Pd, and then the electron-rich state promotes Pd to capture and dissociate molecular hydrogen at low temperatures. As a result, the synergistic effect of lattice stress and electron modification further shifts the critical temperature of "reverse sensing behaviour" of the PdCo NWs towards lower temperatures.

Conclusions

To sum up, low-temperature hydrogen sensors were successfully built with PdCo NWs that show high stability over wide temperature range. The optimized low-temperature stability is achieved by using AAO-confined electrodeposition to modulate the Co content in PdCo NWs to further tune the electronic d-bands of Pd. Remarkably, the PdCo NWs sensors show lower critical temperatures related to the "reverse sensing behavior" ($Pd_{82}Co_{18}$: T_c = 194 K; $Pd_{63}Co_{37}$: T_c = 180 K; $Pd_{33}Co_{67}$: T_c = 184 K) compared to pristine Pd NWs (T_c = 287 K), which greatly expands the low-temperature range of hydrogen detection. The superior sensing stability arises from alloying Pd with Co that generates lattice contraction and electron interaction in NWs, which play crucial roles in suppressing hydrogen brittleness and the α-β phase transitions. Furthermore, we interpret the "reverse sensing behavior" at low temperature with the α-β phase transitions model. This study demonstrates the potential feasibility of tuning the chemical contents in Pd sensing materials for improving hydrogen-sensing stability at low temperature. Such sensors have great potential in future Internet of things.

Conflicts of interest

There are no conflicts to declare.

Acknowledgements

This work was financially supported by the National Natural Science Foundation of China (Grant No. 21473093), Tianjin Municipal Science and Technology Bureau (Grant No. 18ZXSZSF00070) and the Fundamental Research Funds for the Central Universities, Nankai University (Grant No. 63191745). Prof. Luis F Fonseca is funded by NSF Grant HRF-1736093.

References

1 J. Zhang, G. Chen, K. Mullen and X. Feng, *Adv. Mater.*, 2018, e1800528.
2 Y. Jiao, Y. Zheng, M. Jaroniec and S. Z. Qiao, *Chem. Soc. Rev.*, 2015, **44**, 2060-2086.
3 W. T. Koo, S. Qiao, A. F. Ogata, G. Jha, J. S. Jang, V. T. Chen, I. D. Kim and R. M. Penner, *ACS nano*, 2017, **11**, 9276-9285.
4 C. Kuru, C. Choi, A. Kargar, D. Choi, Y. J. Kim, C. H. Liu, S. Yavuz and S. Jin, *Adv. Sci.*, 2015, **2**, 1500004.
5 C. Wadell, S. Syrenova and C. Langhammer, *ACS Nano*, 2014, **8**, 11925-11940.
6 G. Li, H. Kobayashi, J. M. Taylor, R. Ikeda, Y. Kubota, K. Kato, M. Takata, T. Yamamoto, S. Toh, S. Matsumura and H. Kitagawa, *Nat. Mater.*, 2014, **13**, 802-806.
7 S. Kumar, T. Pavloudis, V. Singh, H. Nguyen, S. Steinhauer, C. Pursell, B. Clemens, J. Kioseoglou, P. Grammatikopoulos and M. Sowwan, *Adv. Energy Mater.*, 2018, **8**, 1701326.
8 A. Chen and C. Ostrom, *Chem. Rev.*, 2015, **115**, 11999-12044.
9 S. Dekura, H. Kobayashi, R. Ikeda, M. Maesato, H. Yoshino, M. Ohba, T. Ishimoto, S. Kawaguchi, Y. Kubota, S. Yoshioka, S. Matsumura, T. Sugiyama and H. Kitagawa, *Angew. Chem.*, 2018, **57**, 9823-9827.
10 F. A. A. Nugroho, I. Darmadi, L. Cusinato, A. Susarrey-Arce, H. Schreuders, L. J. Bannenberg, A. B. da Silva Fanta, S. Kadkhodazadeh, J. B. Wagner, T. J. Antosiewicz, A. Hellman, V. P. Zhdanov, B. Dam and C. Langhammer, *Nat. Mater.*, 2019, **18**, 489-495.
11 Y. T. Pan, X. Yin, K. S. Kwok and H. Yang, *Nano letters*, 2014, **14**, 5953-5959.
12 N. Y. Chan, M. Zhao, J. Huang, K. Au, M. H. Wong, H. M. Yao, W. Lu, Y. Chen, C. W. Ong, H. L. Chan and J. Dai, *Adv. Mater.*, 2014, **26**, 5962-5968.
13 N. J. J. Johnson, B. Lam, B. P. MacLeod, R. S. Sherbo, M. Moreno-Gonzalez, D. K. Fork and C. P. Berlinguette, *Nat. Mater.*, 2019, **18**, 454-458.
14 A. Baldi, T. C. Narayan, A. L. Koh and J. A. Dionne, *Nat. Mater.*, 2014, **13**, 1143-1148.
15 J. Lee, W. Shim, E. Lee, J. S. Noh and W. Lee, *Angew. Chem.*, 2011, **50**, 5301-5305.
16 J. Zhang, X. Liu, G. Neri and N. Pinna, *Adv. Mater.*, 2016, **28**, 795-831.
17 C. Sachs, A. Pundt, R. Kirchheim, M. Winter, M. T. Reetz and D. Fritsch, *Phys. Rev. B*, 2001, **64**, 075408.
18 Y. Pak, N. Lim, Y. Kumaresan, R. Lee, K. Kim, T. H. Kim, S. M. Kim, J. T. Kim, H. Lee, M. H. Ham and G. Y. Jung, *Adv. Mater.*, 2015, **27**, 6945-6952.
19 D. Yang, L. Valentin, J. Carpena, W. Otano, O. Resto and L. F. Fonseca, *Small*, 2013, **9**, 188-192.
20 S. Y. Cho, H. Ahn, K. Park, J. Choi, H. Kang and H. T. Jung, *ACS Sens.*, 2018, **3**, 1876-1883.
21 A. Ulvestad, M. J. Welland, W. Cha, Y. Liu, J. W. Kim, R. Harder, E. Maxey, J. N. Clark, M. J. Highland, H. You, P. Zapol, S. O. Hruszkewycz and G. B. Stephenson, *Nat. Mater.*, 2017, **16**, 565-571.
22 M. Khanuja, B. R. Mehta, P. Agar, P. K. Kulriya and D. K. Avasthi, *J. Appl. Phys.*, 2009, **106**, 093515.

23 T. Xu, M. P. Zach, Z. L. Xiao, D. Rosenmann, U. Welp, W. K. Kwok and G. W. Crabtree, *Appl. Phys. Lett.*, 2005, **86**, 203104.
24 N. A. Al-Mufachi and R. Steinberger-Wilckens, *J. Membr. Sci.*, 2018, **545**, 266-274.
25 R. M. Penner, *Acc. Chem. Res.*, 2017, **50**, 1902-1910.
26 F. Yang, D. K. Taggart and R. M. Penner, *Nano Lett.*, 2009, **9**, 2177-2182.
27 F. Yang, S.-C. Kung, M. Cheng, J. C. Hemminger and R. M. Penner, *ACS Nano*, 2010, **4**, 5233-5244.
28 M. A. Lim, D. H. Kim, C.-O. Park, Y. W. Lee, S. W. Han, Z. Li, R. S. Williams and I. Park, *ACS Nano*, 2012, **6**, 598-608.
29 D. Yang and L. F. Fonseca, *Nano Lett.*, 2013, **13**, 5642-5646.
30 X. Li, Y. Liu, J. C. Hemminger and R. M. Penner, *ACS Nano*, 2015, **9**, 3215-3225.
31 C. G. Sonwane, J. Wilcox and Y. H. Ma, *J. Phys. Chem. B*, 2006, **110**, 24549-24558.
32 F. A. A. Nugroho, I. Darmadi, V. P. Zhdanov and C. Langhammer, *ACS Nano*, 2018, **12**, 9903-9912.
33 J. S. Jang, S. Qiao, S. J. Choi, G. Jha, A. F. Ogata, W. T. Koo, D. H. Kim, I. D. Kim and R. M. Penner, *ACS Appl. Mater. Interfaces*, 2017, **9**, 39464-39474.
34 C. E. Ho, W. Z. Hsieh, P. T. Lee, Y. H. Huang and T. T. Kuo, *Appl. Surf. Sci.*, 2018, **434**, 1353-1360.
35 C. Zhao, A. Goldbach and H. Xu, J. Membr. Sci., 2017, 542, 65-67.
36 M. Weber, J.-Y. Kim, J.-H. Lee, J.-H. Kim, I. Iatsunskyi, E. Coy, P. Miele, M. Bechelany and S. S. Kim, *J. Mater. Chem. A*, 2019, **7**, 8107-8116.
37 X.-T. Yin, W.-D. Zhou, J. Li, Q. Wang, F.-Y. Wu, D. Dastan, D. Wang, H. Garmestani, X.-M. Wang and Ş. Ţălu, *J. Alloys Compd.*, 2019, **805**, 229-236.
38 X.-T. Yin, W.-D. Zhou, J. Li, P. Lv, Q. Wang, D. Wang, F.-y. Wu, D. Dastan, H. Garmestani, Z. Shi and Ş. Ţălu, *J. Mater. Sci.: Mater. Electron.*, 2019, **30**, 14687-14694.
39 M. Weber, J. H. Kim, J. H. Lee, J. Y. Kim, I. Iatsunskyi, E. Coy, M. Drobek, A. Julbe, M. Bechelany and S. S. Kim, *ACS Appl. Mater. Interfaces*, 2018, **10**, 34765-34773.
40 D. Dastan, P. U. Londhe and N. B. Chaure, *J. Mater. Sci.: Mater. Electron.*, 2014, **25**, 3473-3479.
41 D. Dastan, N. Chaure and M. Kartha, *J. Mater. Sci.: Mater. Electron.*, 2017, **28**, 7784-7796.
42 S. K. Sengar, B. R. Mehta and G. Gupta, *Appl. Phys. Lett.*, 2011, **98**, 193115.
43 A. Pozio, Z. Jovanović, R. Lo Presti, M. De Francesco and S. Tosti, *Int. J. Hydrogen Energy*, 2012, **37**, 7925-7933.
44 D. Yang, J. Carpena-Nunez, L. F. Fonseca, A. Biaggi-Labiosa and G. W. Hunter, *Sci. Rep.*, 2014, **4**, 3773.
45 L. Du, L. Zheng, H. Wei, S. Zheng, Z. Zhu, J. Chen and D. Yang, *ACS Appl. Nano Mater.*, 2019, **2**, 1178-1184.